ARTICLE IN PRESS

Available online at www.sciencedirect.com
SCIENCE DIRECT®

ELSEVIER

International Journal of Solids and Structures xxx (2006) xxx–xxx

INTERNATIONAL JOURNAL OF SOLIDS and STRUCTURES

www.elsevier.com/locate/ijsolstr

Large-scale failure modes of dielectric elastomer actuators

Jean-Sébastien Plante *, Steven Dubowsky

Field and Space Robotics Laboratory, Department of Mechanical Engineering, Room 3-469, Massachusetts Institute of Technology, 77 Massachusetts Avenue, Cambridge, MA 02139, USA

Received 9 January 2006; received in revised form 9 March 2006

Abstract

Dielectric elastomer actuators (DEAs) show promise for robotic and mechatronic applications. However, to date, these actuators have experienced high rates of failure that have prevented their practical application. Here, large scale modes of failure of DEAs and their performance limits are studied. The objective is to provide design guidelines and bound the performance of DEAs that avoid failure. An idealized DEA is modeled and its failure is predicted as a function of film pre-stretch used during actuator fabrication, actuation voltage, and stretch rate. Three failure modes are considered: pull-in, dielectric strength, and material strength. Each failure mode is shown to dominate for different combinations of pre-stretch and stretch rate. High stretch rates lead to dielectric strength failure while low stretch rates lead to pull-in failure. Material strength failure is less important for most cases. Model predictions are validated experimentally using practical DEAs operating under load. This study suggests that DEAs cannot be operated reliably under load for long periods of time or low stretch rates due to pull-in failure limitations. To be reliable, DEAs must be used for short periods of time with high stretch rates.

Keywords: Dielectric; Elastomer; Failure; Performance; Fundamental; Model

1. Introduction

Dielectric elastomer actuators (DEAs) represent a promising alternative to existing large displacement actuators for use in mechatronic devices such as DC motors and pneumatic or hydraulic cylinders. They are simple, potentially low cost, and lightweight, see Kornbluh et al. (1995), Pelrine et al. (1998), Kornbluh et al. (1999), Wingert (2002), Wingert et al. (2002a,b). DEAs consist of an elastomeric film (thickness ≈ 100 μm) coated on both sides with compliant electrodes, see Fig. 1. Maxwell stresses are generated in the film when a differential voltage is applied across the two compliant electrodes. The resulting film thickness reduction causes the film to expand in area. The film is kept in tension (to prevent buckling) by *pre-stretching* it. The tensile loading due to the initial pre-stretching of the film plays a fundamental role in the actuator design by significantly affecting the film properties.

* Corresponding author. Tel.: +1 617 253 5592; fax: +1 617 258 7881.
E-mail address: jsplante@mit.edu (J.-S. Plante).

0020-7683/$ - see front matter © 2006 Elsevier Ltd. All rights reserved.
doi:10.1016/j.ijsolstr.2006.03.026

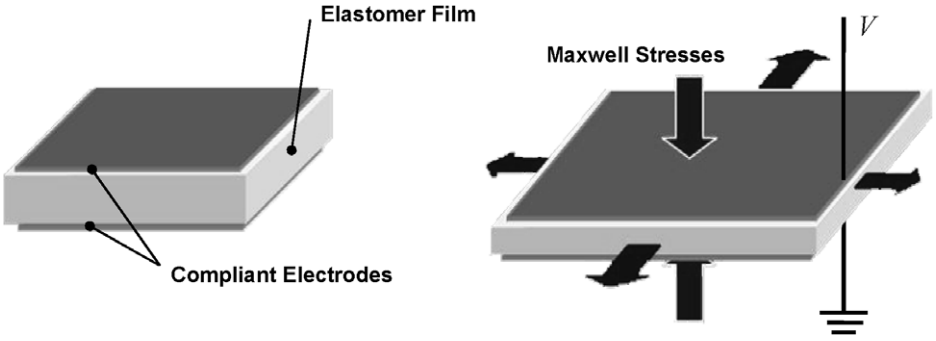

Fig. 1. DEA operating principle. Adapted from Wingert (2002).

A number of different DEA designs have been implemented in the past decade, see for example: Kornbluh et al. (1995), Pelrine et al. (1998), Wingert et al. (2002b), Pei et al. (2003), Vogan et al. (2004) and Plante et al. (2005). Some of these proof-of-concept actuators have shown extensions up to three times their initial lengths, acceptable efficiencies and specific energy densities. However, our experimental work has shown that actuator life is a serious concern. In order for this technology to be practical, dielectric elastomer actuation needs to be robust, reliable, and long lived. To date, little research has addressed these issues. The objective of this paper is to understand the nature of DEA failure with respect to their working conditions and to bound the performance in order to avoid failure.

1.1. Background

The first physical models of DEAs developed by Kornbluh et al. (1995) and Pelrine et al. (1998) suggested that the effect of the Maxwell stresses can be lumped into an equivalent Maxwell pressure, P, given by:

$$P = -\varepsilon_d \varepsilon_0 \left(\frac{V}{t}\right)^2 \tag{1}$$

where ε_0 is the permittivity of free space (8.85×10^{-12} F/m), ε_d is the material dielectric constant, V is the voltage applied across the electrodes, and t is the thickness of the actuated film. The minus sign indicates that the equivalent pressure is compressive.

Eq. (1) is valid for uniform electrical charge distribution on infinitely large electrodes and uniform film thickness. Kofod and Sommer-Larsen (2005) experimentally verified the validity of Eq. (1) for DEAs. The simplicity and accuracy of Eq. (1) makes it the generally accepted electromechanical coupling model for DEAs. It should be noted that Eq. (1) represents only an approximation of the real film loading. McMeeking and Landis (2005) have addressed some of the details of the complete electromechanical coupling.

Early failure analysis done by Pelrine et al. (1998), Kornbluh et al. (1999), and Sommer-Larsen et al. (2001) used linear (Hookean) stress/strain relationships to investigate a failure mode known as *pull-in* failure. A pull-in failure occurs when the film thickness falls below a certain threshold and the equivalent Maxwell pressure becomes always greater than the compressive stress of the elastomer film. This positive feedback leads to an unstable compression of the elastomer material with catastrophic failure. In these studies, the one-dimensional models with linear stress/strain relationships predicted pull-in threshold values of about half of the extensions reported in the literature, see for example Pei et al. (2003) and Plante et al. (2005). Hence, linear models are inadequate to deal with the significant nonlinear behavior of DEAs (large deformation and nonlinear elasticity).

Analytical methods that account for large deformation and nonlinear elastic properties have been used widely in the field of continuum mechanics, see for example Ogden (1984), Anand (1996), Holzapfel (2000), and Anand and Gurtin (2003). Researchers including Pelrine et al. (2000a), Kofod (2001), and Goulbourne et al. (2003, 2004) have successfully applied such continuum models for hyper-elastic materials to DEAs but have not studied their failure modes.

The viscoelastic behavior of DEA films has been investigated by Larsen et al. (2002) using a Mooney–Rivlin model with Maxwell viscosity. This model was applied to a film element made of VHB 4905/4910 under uniaxial extension of 1.8 times its initial length. Other similar studies were conducted by Yang et al. (2005) up to stretches of 3.0. These models did not address failure and used stretches substantially lower than those found in typical DEA applications, which can be as high as 5.0.

Recently, Wissler and Mazza (2005) studied the deformation of dielectric elastomer circles using various hyper-elastic models coupled with quasi-linear viscoelasticity within finite element models. These models were not validated over a wide range of experimental parameters and suggested pull-in failure is not a concern for DEA, which contradicts experimental observations presented here. Hence, the role of viscoelasticity on DEA failure modes was not completely understood.

Other constitutive models of nonlinear viscoelastic materials undergoing large deformation have been developed but have not been applied to DEA materials, for example: Bergström and Boyce (1998, 2000) and Drozdov and Dorfmann (2002).

The role of film dielectric strength on extension performance of DEA was studied by Sommer-Larsen et al. (2001) and its important effect on DEA extension is illustrated by a figure of merit:

$$\lambda \propto \frac{E^2}{Y} \tag{2}$$

where λ is the actuator's output stretch, E is the maximum electric field or dielectric strength, and Y is the apparent Young's modulus. Since the dielectric strength is squared, it strongly affects DEA performance limits. Pelrine et al. (2000b) and Kofod et al. (2001) showed the dielectric strength of VHB 4905/4910 to increase from about 40 MV/m to 240 MV/m when stretched to 36 times its initial area, a major variation when viewed in light of Eq. (2). However, models have not yet been developed that include this effect to predict DEA failure.

In summary, to predict DEA failure modes, the models need to include the effects of very large deformations, nonlinear elastic behavior, viscoelasticity, and variable dielectric strength.

1.2. Approach

This paper presents an analytical model of dielectric elastomer actuation that incorporates these four fundamentals effects. The model predicts DEA area expansion (stretch) as a function of film mechanical pre-stretch, applied voltage, speed of actuation (stretch rate), and working load. Viscoelastic effects are included by defining hyper-elastic models from experimental data obtained a various stretch rates. The analysis does not include localized effects such as defects, voids, inclusions, mechanical stress concentration, electric field concentration and time dependent failures such as creep or fatigue. These local failure modes are considered in Vogan (2004) and Plante (2006).

The model is then used to investigate three failure modes of DEAs made from VHB 4905/4910 elastomer: (1) pull-in, (2) dielectric strength and (3) material strength. Experimental data validates the model performance at both low and high stretch rates for a class of practical DEA (diamond actuators) operating under working loads. It is shown that the effect of working load on actuator failure is very substantial and cannot be ignored as in many past studies that addressed DEA failure, like Pelrine et al. (1998), Kornbluh et al. (1999), Sommer-Larsen et al. (2001), and Wissler and Mazza (2005). It is also shown that, due to the film's viscoelasticity, each failure mode dominates under different conditions of stretch rates. At high stretch rates, dielectric strength is the dominant mode of failure. At low stretch rates, pull-in is the dominant mode of failure. An important practical result of this study is that DEAs made from VHB 4905/4910 elastomer can reliably achieve large working loads at large extensions only if operating at high stretch rates.

2. Analytical model development

2.1. Problem definition

The majority of DEA designs are variants of what can be called rolled and planar classes, see Pelrine et al. (2001), Kornbluh et al. (2002), Wingert et al. (2002a,b), Pei et al. (2004), and Plante et al. (2005). These designs

provide good mechanical energy conversion, but as pointed out by Pei et al. (2004) and Plante et al. (2005), they are sensitive to localized failure modes such as stress concentrations at the film bonding interface. To minimize these local effects, this study develops a basic actuation model based on a *circular actuator* that consists of a small conductive circle located in the center of a large pre-stretched film as shown in Fig. 2. Under Maxwell pressure, the expanding circle's radius increases from its pre-stretched value, r_{pre}, to its actuated value, r_{act}. The film deformation of this circular actuator occurs far from the film's rigid ring ($r_{\text{rig}} > r_{\text{act}}$) and local failures due to the film bonding interface are minimized; putting emphasis on fundamental or large-scale failure modes. Local failure modes are addressed by Vogan (2004) and Plante (2006).

The circular actuator model considers the following: very large deformations, nonlinear elastic behavior, viscoelasticity, working loads, and varying dielectric strength. The analysis is based on the following assumptions and restrictions:

- The study focuses on VHB 4905/4910 elastomer because, to date, it gives the largest displacements and work outputs of all tested materials, see for example Cameron et al. (2004), Kornbluh et al. (1995, 1999, 2000), Sommer-Larsen and Ladeggard Larsen (2004). Also, this material is commercially available as an adhesive tape that does not require elaborate fabrication processes.
- The film is modeled as a hyper-elastic material. The film's viscoelasticity is included in the analysis by defining two elastic material models at two highly different stretch rates. The parameters of these models are defined under uniaxial extensions of: $\dot{\lambda}_{\text{UNI}} = 3.3 \times 10^{-4}\ \text{s}^{-1}$ and $0.094\ \text{s}^{-1}$ (see Appendix A). The low stretch rate of $\dot{\lambda}_{\text{UNI}} = 3.3 \times 10^{-4}\ \text{s}^{-1}$ is taken as the quasi-equilibrium stretch rate where viscoelastic effects are small enough to be negligible (see Appendix A). The high stretch rate of $\dot{\lambda}_{\text{UNI}} = 0.094\ \text{s}^{-1}$ is typical of many robotics and mechatronics applications. The analysis is limited to these two stretch rates and all deformations are assumed to take place at constant stretch rates. Compared to constitutive viscoelastic modeling, the proposed approach is simpler and, as shown in Section 4, presents useful results for unidirectional stretches up to 6.0.

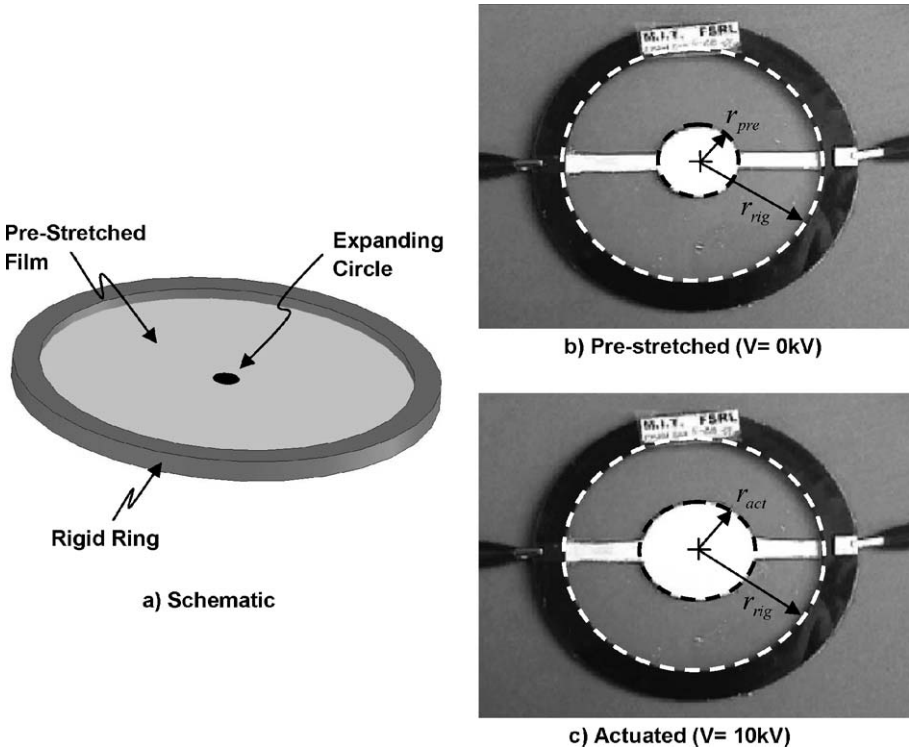

Fig. 2. Circular actuator.

- The film is incompressible. The rubber-like material VHB 4905/4910 used here has a Poisson's ratio of 0.49, which is very close to the incompressible value of 0.5, see 3M (2001).
- The film mechanical properties are isotropic before pre-stretching (verified experimentally up to stretches of 7).
- Equivalent Maxwell stress predictions are made using a dielectric constant for VHB 4905/4910 films of $\varepsilon_d = 4.5$. Kofod et al. (2001) showed good prediction performance with this value.
- Circular actuators cannot provide mechanical work because they have no physical connections to outside systems. Nonetheless, the effect of working loads is included in the analysis by superposing a radial loading stress acting around the expanding circle's perimeter to block its expansion. Typical loading stress values are estimated from practical actuators called *diamond actuators* such as shown in Fig. 3.
- The dimensions of the studied circular actuator (see Fig. 2) are kept constant at: $r_{pre} = 5.6$ mm and $r_{rig} = 100$ mm. With these proportions, the expanding circle is small compared to the rigid ring and the film can be viewed as quasi-infinite. The effect of radii proportions on failure is not studied.

The objective of the circular actuator model is to find the actuation stretches, $\lambda_{i,act}$, for any given voltage, V, mechanical pre-stretch, $\lambda_{i,pre}$, constitutive model stretch rate, $\dot{\lambda}_{UNI}$, and loading stress, σ_{load}:

$$\lambda_{i,act} = f(V, \lambda_{i,pre}, \dot{\lambda}_{UNI}, \sigma_{load}) \tag{3}$$

The model to be developed here will not have an explicit closed-form solution; therefore the actuation stretches, $\lambda_{i,act}$, given by Eq. (3) will be solved numerically.

The circular actuator model is separated into two distinct regions: the *active region* and the *passive region*, see Fig. 4. Each region is modeled separately and boundary conditions are applied between the two. The model and the failure criteria are developed in the following sections.

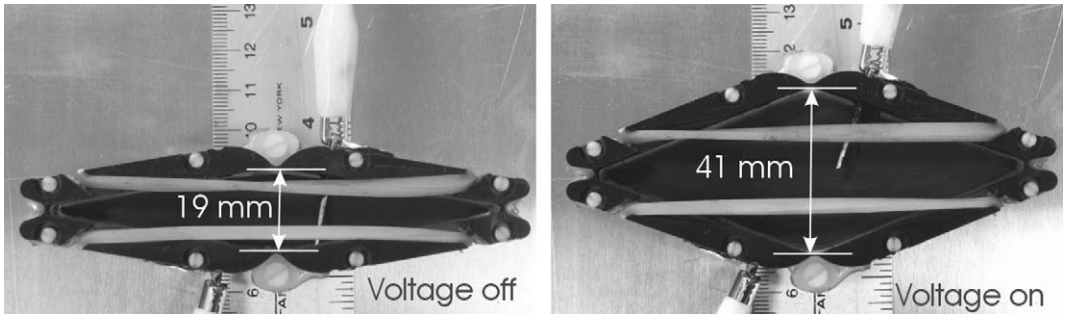

Fig. 3. Diamond actuator showing linear extensions of 100%.

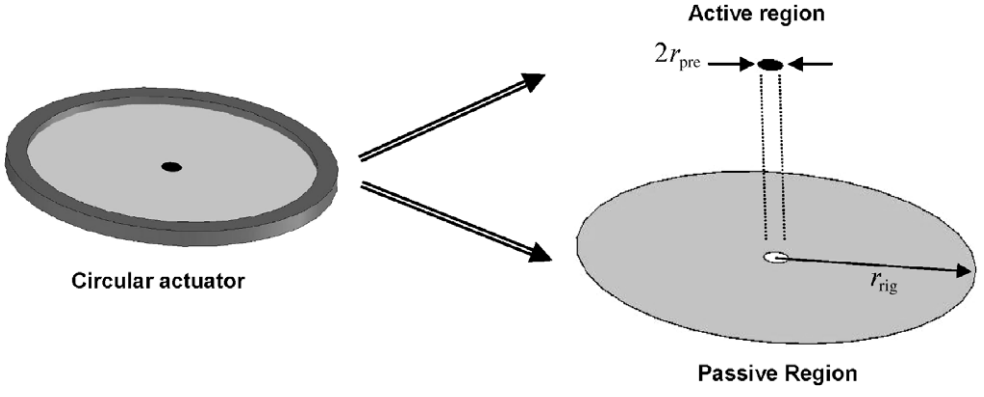

Fig. 4. Circular actuator decomposed into active and passive regions.

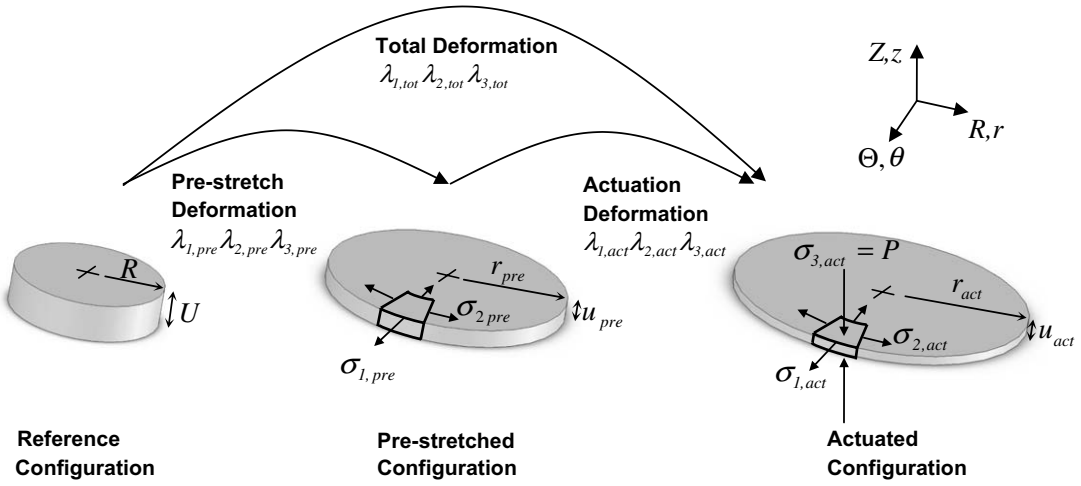

Fig. 5. The deformations and stresses of the active region.

2.2. Active region

2.2.1. Kinematical description

The deformations of the active region and its key parameters are illustrated in Fig. 5. The *total deformation* is decomposed in two separate and consecutive deformations: the *pre-stretch deformation* and the *actuation deformation*. Fig. 5 shows how the active region's radius and thickness evolve from the *reference configuration*, R, U, to the *pre-stretched configuration*, $r_{\text{pre}}, u_{\text{pre}}$, and finally to the *actuated configuration*, $r_{\text{act}}, u_{\text{act}}$. The dimensions in the reference configuration are expressed in the R, Θ, Z system while those of the pre-stretched and actuated dimensions are expressed in the r, θ, z system. The active region experiences a *pure stretch* deformation (no angular or shear deformations), and the r, θ, z directions of Fig. 5 coincide with the principal stresses and stretches directions denoted by the indices 1, 2, 3. Under these conditions, the principal stretches of the pre-stretch (pre), actuation (act) and total (tot) deformations of the active region are defined from the following dimensionless ratios (see Fig. 5):

$$\lambda_{1,\text{pre}} = \lambda_{2,\text{pre}} = \frac{r_{\text{pre}}}{R} \quad \lambda_{3,\text{pre}} = \frac{u_{\text{pre}}}{U} \tag{4}$$

$$\lambda_{1,\text{act}} = \lambda_{2,\text{act}} = \frac{r_{\text{act}}}{r_{\text{pre}}} \quad \lambda_{3,\text{act}} = \frac{u_{\text{act}}}{u_{\text{pre}}} \tag{5}$$

$$\lambda_{1,\text{tot}} = \lambda_{2,\text{tot}} = \lambda_{2,\text{pre}}\lambda_{2,\text{act}} \quad \lambda_{3,\text{tot}} = \lambda_{3,\text{pre}}\lambda_{3,\text{act}} \tag{6}$$

The pre-stretches are equibiaxial: $\lambda_{1,\text{pre}} = \lambda_{2,\text{pre}}$. Equibiaxial pre-stretches combined with the material's isotropy (before pre-stretching) and the system's axisymmetry ensure that the actuation deformation is also equibiaxial: $\lambda_{1,\text{act}} = \lambda_{2,\text{act}}$. The kinematical description is reduced to a single unknown principal stretch for each deformation by making use of the incompressibility assumption ($\det\mathbf{F} = J = 1$), which imply the product of the principal stretches to be one for all deformations:

$$\lambda_{1,\text{pre}}\lambda_{2,\text{pre}}\lambda_{3,\text{pre}} = \lambda_{1,\text{act}}\lambda_{2,\text{act}}\lambda_{3,\text{act}} = \lambda_{1,\text{tot}}\lambda_{2,\text{tot}}\lambda_{3,\text{tot}} = 1 \tag{7}$$

2.2.2. Stress balance

As shown in Fig. 5, the pre-stretch deformation creates principal stresses[1] in the pre-stretched configuration, $\sigma_{1,\text{pre}}$, $\sigma_{2,\text{pre}}$, $\sigma_{3,\text{pre}}$. The pre-stretched configuration is then perturbed by the equivalent Maxwell pressure,

[1] In this paper, "true" stresses or Cauchy stresses are identified by "σ" while engineering stresses or First Piola–Kirchoff stresses are identified by "S". The difference is the area "A" defining the stress: one is expressed in the reference configuration: $S = F/A_{\text{reference}}$, and the other in a deformed configuration: $\sigma = F/A_{\text{deformed}}$.

P, resulting from voltage application. The film further deforms and the principal stresses in the actuated configuration reach a new equilibrium to $\sigma_{1,\mathrm{act}}$, $\sigma_{2,\mathrm{act}}$, $\sigma_{3,\mathrm{act}}$.

The actuation stretches, $\lambda_{i,\mathrm{act}}$, are reached when the equivalent Maxwell pressure, P, of Eq. (1) is in equilibrium with the active region's third principal stress:

$$P(V, \lambda_{i,\mathrm{pre}}, \lambda_{i,\mathrm{act}}) = \sigma_{3,\mathrm{act}}(\lambda_{i,\mathrm{pre}}, \lambda_{i,\mathrm{act}}) \quad i = 1, 2, 3 \tag{8}$$

The third principal stress, $\sigma_{3,\mathrm{act}}$, is found from a stress/stretch constitutive model based on Ogden's formulation for rubbery materials, see Ogden (1972, 1982). Ogden's model defines a material's Helmoltz free-energy[2] by:

$$\psi = \tilde{\psi}(\lambda_1, \lambda_2, \lambda_3) = \sum_{p=1}^{N} \frac{\mu_p}{\alpha_p}(\lambda_1^{\alpha_p} + \lambda_2^{\alpha_p} + \lambda_3^{\alpha_p} - 3) \tag{9}$$

where μ_p and α_p are experimentally determined material parameters and N is the model order (see Appendix A). Kofod (2001) used a second order model for VHB 4905/4910 with good prediction capabilities.

Taking the derivative of the Helmoltz free energy function of Eq. (9) with respect to the deformation gradient tensor leads to the constitutive stress/stretch formulation in the reference configuration (Holzapfel, 2000):

$$S_i = -\left(\frac{p}{\lambda_i}\right) + \sum_{p=1}^{2} \mu_p \lambda_i^{(\alpha_p - 1)} \quad i = 1, 2, 3 \tag{10}$$

where p is a Lagrange multiplier defined by the boundary conditions. Physically, p can be viewed as a hydrostatic pressure.

The Piola transformation between the engineering stress (reference configuration) and true stress (deformed configuration) tensors is given by (Holzapfel, 2000):

$$\boldsymbol{\sigma} = J^{-1}\mathbf{S}\mathbf{F}^{\mathrm{T}} \tag{11}$$

where $\boldsymbol{\sigma}$ is the true stress tensor and $\mathbf{S}$ is the engineering stress tensor. For incompressible materials ($\det \mathbf{F} = J = 1$) under pure stretch deformations, Eq. (11) written in components reduces to:

$$\sigma_i = S_i \lambda_i \quad i = 1, 2, 3 \tag{12}$$

Applying the Piola transformation to Eq. (10) yields:

$$\sigma_i = -p + \sum_{p=1}^{2} \mu_p \lambda_i^{\alpha_p} \quad i = 1, 2, 3 \tag{13}$$

Eq. (13) written for the active region in the actuated configuration gives:

$$\begin{aligned} \sigma_{1,\mathrm{act}} &= -p + \mu_1 \lambda_{1,\mathrm{tot}}^{(\alpha_1)} + \mu_2 \lambda_{1,\mathrm{tot}}^{(\alpha_2)} \\ \sigma_{2,\mathrm{act}} &= \sigma_{1,\mathrm{act}} \\ \sigma_{3,\mathrm{act}} &= -p + \mu_1 \lambda_{3,\mathrm{tot}}^{(\alpha_1)} + \mu_2 \lambda_{3,\mathrm{tot}}^{(\alpha_2)} \end{aligned} \tag{14}$$

The first principal stress, $\sigma_{1,\mathrm{act}}$, of Eq. (14) defines the hydrostatic pressure, p:

$$p = \mu_1 \lambda_{1,\mathrm{tot}}^{(\alpha_1)} + \mu_2 \lambda_{1,\mathrm{tot}}^{(\alpha_2)} - \sigma_{1,\mathrm{act}} \tag{15}$$

which is inserted back into the third principal stress:

$$\sigma_{3,\mathrm{act}} = \sigma_{1,\mathrm{act}} - (\mu_1 \lambda_{1,\mathrm{tot}}^{(\alpha_1)} + \mu_2 \lambda_{1,\mathrm{tot}}^{(\alpha_2)}) + (\mu_1 \lambda_{3,\mathrm{tot}}^{(\alpha_1)} + \mu_2 \lambda_{3,\mathrm{tot}}^{(\alpha_2)}) \tag{16}$$

The numerical value of the first principal stress, $\sigma_{1,\mathrm{act}}$, is determined from the boundary condition between the active and passive regions.

[2] For hyper-elastic materials, the Helmoltz free-energy only depends on the deformation of the material and is therefore sometimes called the strain-energy function.

2.3. Passive region

2.3.1. Kinematical description

The stresses and stretches of the passive region are not uniform. The passive region is modeled as an annular membrane with imposed inner and outer radial displacements. This approach allows solving a 1D axisymmetric problem and is convenient to the present analysis that studies widely varying input conditions (stretch rate, load, pre-stretch). The development is based on the general membrane analysis proposed by Yang and Feng (1970). Yang et al. (2005) also presented a treatment of annular dielectric elastomer membranes. Fig. 6 shows a cross-section of the passive region with associated radial dimensions in the reference (stress free) and actuated configurations.

The membrane assumption only allows one principal stretch to be matched at its boundaries (otherwise the problem is 2D axisymmetric). This limitation results in a thickness discontinuity at the interface with the active region and is accounted for by developing an empirical boundary condition.

In the passive region problem, the relevant principal stretch to match is the radial one. The membrane's initial radii, R_a and R_b, are thus imposed to assure radial continuity with the active region and rigid ring. The inner radius, R_a, projected in the pre-stretched configuration must be equal to the active region's radius $R_a\,\lambda_{1,pre} = r_{pre}$ (see Fig. 4). Similarly, the outer radius, R_b, projected in the pre-stretched configuration must be equal to the rigid rings' radius $R_b\lambda_{1,pre} = r_{rig}$. These conditions lead to:

$$\begin{aligned} R_a &= \frac{r_{pre}}{\lambda_{1,pre}} \\ R_b &= \frac{r_{rig}}{\lambda_{1,pre}} \end{aligned} \tag{17}$$

The principal stretches of an annular membrane in the 1, 2, 3 directions (corresponding to the r,θ,z and R,Θ,Z directions) are:

$$\begin{aligned} \lambda_1 &= \frac{\partial r}{\partial R} \\ \lambda_2 &= \frac{r}{R} \\ \lambda_3 &= \frac{1}{\lambda_1\lambda_2} \end{aligned} \tag{18}$$

where λ_3 is obtained from the incompressibility relation: $\lambda_1\lambda_2\lambda_3 = 1$.

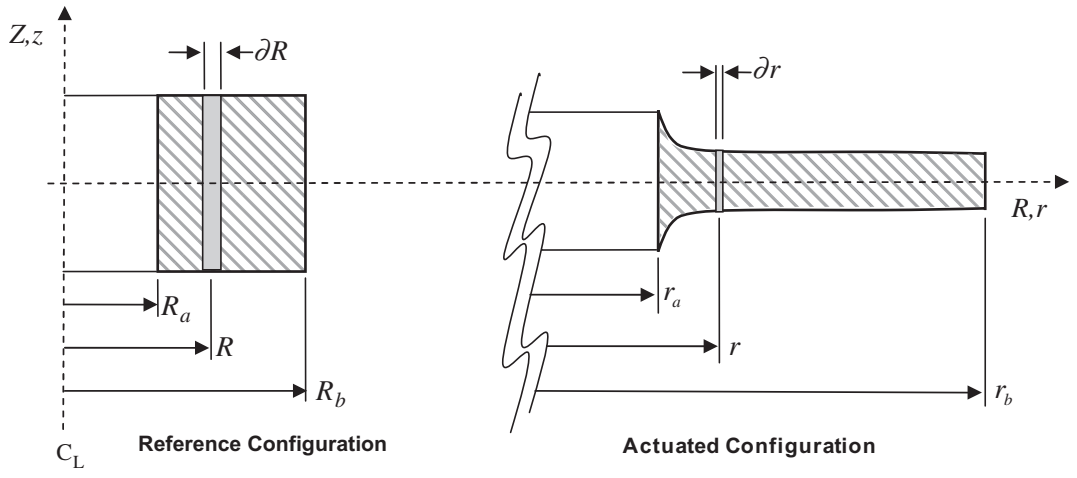

Fig. 6. Deformation of the passive region model.

2.3.2. Stress balance

The principal stresses associated with the principal directions must satisfy Cauchy's equation of equilibrium, $\operatorname{div}\boldsymbol{\sigma} = \mathbf{0}$. This equation resolved in the actuated configuration reduces to:

$$\frac{\partial \sigma_1}{\partial r} + \frac{1}{r}(\sigma_1 - \sigma_2) = 0 \tag{19}$$

Eqs. (18) and (19) are combined into two first order differential equations:

$$\begin{aligned} \frac{\partial \lambda_1}{\partial R} &= \frac{\lambda_1}{R\lambda_2} \cdot \frac{\sigma_2 - \sigma_1}{\dfrac{\partial \sigma_1}{\partial \lambda_1}} - \frac{\lambda_1 - \lambda_2}{R} \cdot \frac{\dfrac{\partial \sigma_1}{\partial \lambda_2}}{\dfrac{\partial \sigma_1}{\partial \lambda_1}} \\ \frac{\partial \lambda_2}{\partial R} &= \frac{\lambda_1 - \lambda_2}{R} \end{aligned} \tag{20}$$

where the principal stresses are found from a second order Ogden model given by:

$$\begin{aligned} \sigma_1 &= \mu_1\left((\lambda_1)^{\alpha_1} - \frac{1}{(\lambda_1)^{\alpha_1}(\lambda_2)^{\alpha_1}}\right) + \mu_2\left((\lambda_1)^{\alpha_2} - \frac{1}{(\lambda_1)^{\alpha_2}(\lambda_2)^{\alpha_2}}\right) \\ \sigma_2 &= \mu_1\left((\lambda_2)^{\alpha_1} - \frac{1}{(\lambda_1)^{\alpha_1}(\lambda_2)^{\alpha_1}}\right) + \mu_2\left((\lambda_2)^{\alpha_2} - \frac{1}{(\lambda_1)^{\alpha_2}(\lambda_2)^{\alpha_2}}\right) \\ \sigma_3 &= 0 \end{aligned} \tag{21}$$

The pair of differential equations of Eq. (20) is solved numerically by transforming the boundary value problem into an initial condition problem as suggested by Yang and Feng (1970). In the transformed problem, the stretches are calculated iteratively from the inner radius R_a to the outer radius R_b until the calculated outer radius (in the actuated configuration) converges to the rigid ring radius $r_b = r_{rig}$. The inner hoop stretch λ_2 is equal to the active region's value: $\lambda_2 = \lambda_{2,tot}$. The inner radial stretch λ_1 is unknown and is the iterated variable.

2.3.3. Solution example

Consider a film pre-stretched to $\lambda_{1,pre} = 1.96$ and actuated to $\lambda_{1,act} = 2$. The calculated principal stretches and stresses are shown, respectively, in Figs. 7 and 8. Compared to the pre-stretched configuration, Fig. 7 shows that, near the inside radius, R_a, the polymer chains in the hoop direction are further extended $\lambda_1 > \lambda_{1,pre}$ while those in the radial direction are relaxed, $\lambda_2 < \lambda_{1,pre}$. Accordingly, Fig. 8 shows that the second principal stress (hoop) increase while the first principal stress (radial) decrease. The stresses and stretches both rapidly converge toward the pre-stretched values in the far field when $R \to R_b$. Fig. 9 shows the predicted deformed shape of the active/passive regions interface using the membrane approximation.

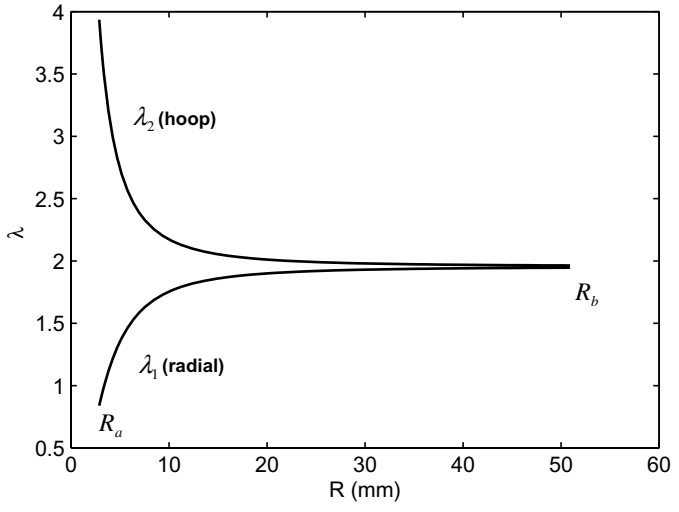

Fig. 7. Example of stretch distribution in the passive region.

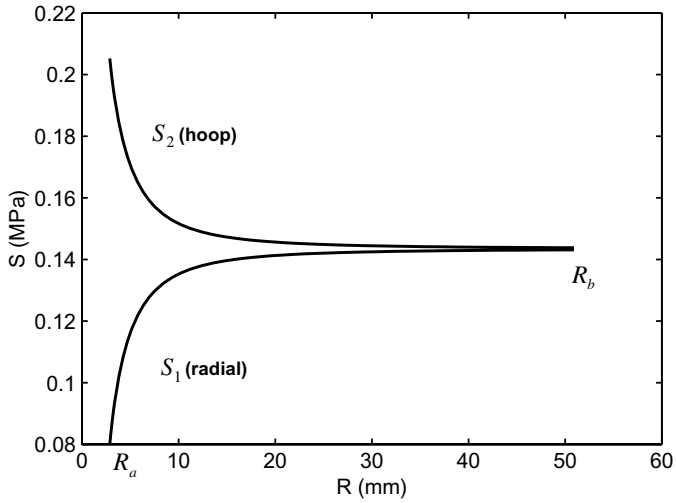

Fig. 8. Example of engineering stress distribution in the passive region.

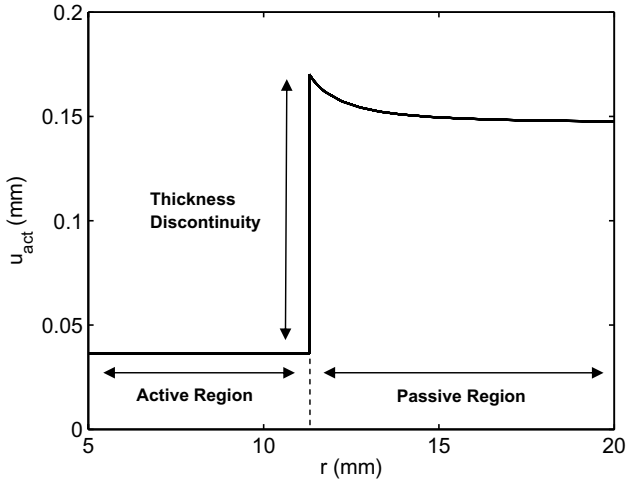

Fig. 9. Example of deformed shape showing thickness discontinuity between active and passive regions (not to scale).

2.4. Boundary condition

The thickness discontinuity at the active/passive regions interface resulting from the membrane approximation (see Fig. 9) does not faithfully represent the true deformed shape which is continuous. The continuous case implies extra material deformation to force the edges of the active and passive region together. This extra energy must come from higher Maxwell pressures, and higher Maxwell pressures means *lower* (more compressive) first principal stresses in the active region.

A finite element (FE) model of the passive region was developed to study the effect of the thickness discontinuity. The FE model was implemented in Adina® using axisymmetric 2D Solid elements and the Ogden material model parameters for high stretch rates ($\dot{\lambda}_{\mathrm{UNI}} = 0.094\ \mathrm{s}^{-1}$), see Appendix A. Both the membrane (discontinuous) and continuous cases were run with pre-stretches of $\lambda_{1,\mathrm{pre}} = 1.96$ and actuation stretches of $\lambda_{1,\mathrm{act}} = 1.05$, 1.2, 2 and 3. The resulting deformed shapes for both cases are shown in Fig. 10 for $\lambda_{1,\mathrm{act}} = 2$.

The FE simulation results were used to compute the active region's first principal stress for the discontinuous and continuous cases. Results are shown in Fig. 11. Looking at the FE results only, as expected, the first principal stress decreases significantly faster in the continuous case because it requires more deformation

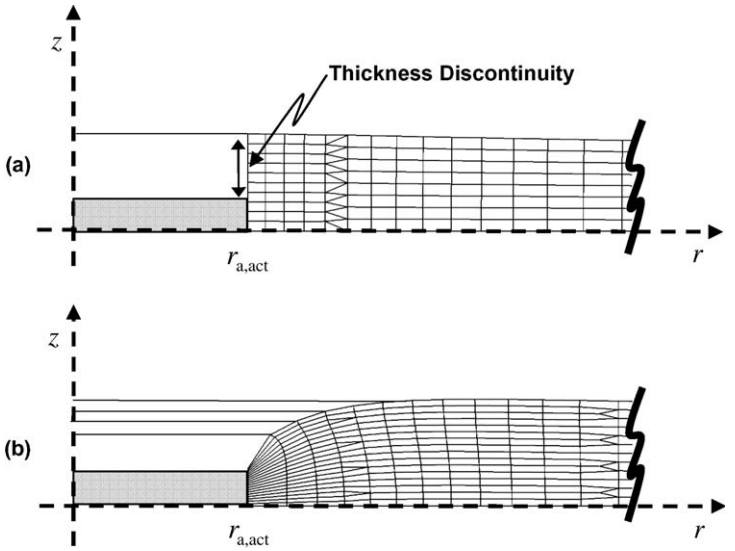

Fig. 10. Passive region's deformed shape computed with FE models when inner face is: (a) discontinuous and (b) continuous (not to scale).

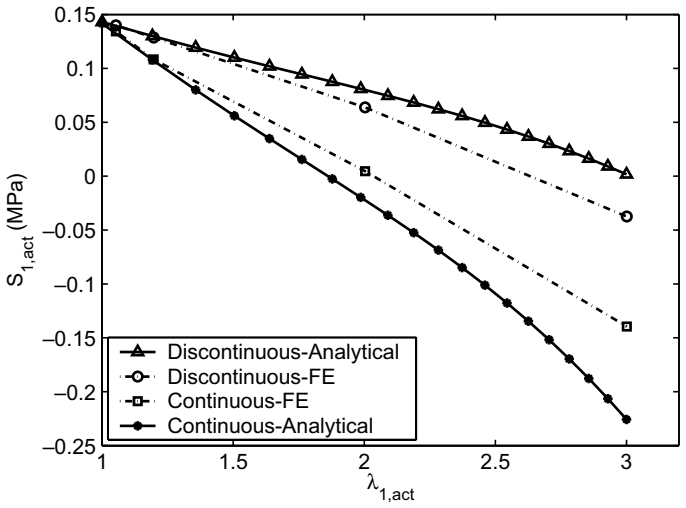

Fig. 11. Active region planar stress in function of actuation stretch for analytical and FE models.

energy. The Continuous-FE case of Fig. 11 is closer to the true continuous interface geometry and is set as the reference case that should be matched by the circular actuator model.

Fig. 11 shows negative first principal stresses at large actuation stretches. When such negative values are reached, the film theoretically buckles out of plane in a complex 3D shape. These deformations are not handled by the models presented here. In practice, rare buckling occurrences of circular actuators can be observed at low pre-stretches, typically for $\lambda_{1,pre} < 2$. This limitation is not expected to have a significant impact on the results of this study.

The FE results of Fig. 11 are now used as benchmarks for two analytical solutions of the passive region's membrane model using different boundary conditions.

The first solution is the Discontinuous-Analytical, see Fig. 11, and its purpose is to assess the validity of the membrane approximation. The membrane model and Discontinuous-FE cases both show discontinuous interfaces and should therefore develop similar first principal stresses. The boundary condition is found from

a radial force balance across the interface leading to equal first principal stresses in the reference configuration:

$$S_{\substack{1,\mathrm{act}\\ \mathrm{discontinuous}}} = S_1(R_a) \tag{22}$$

where $S_{\substack{1,\mathrm{act}\\ \mathrm{discontinuous}}}$ is the first principal stress in the active region and $S_1(R_a)$ is the first principal stress of the passive region at the inner radius. As shown by Fig. 11, the Discontinuous-Analytical solution using Eq. (22) matches the Discontinuous-FE case reasonably well. This suggests that the membrane model yields valid results.

The second solution is the Continuous-Analytical, see Fig. 11, and its purpose is to match the stress level of the Continuous-FE case, the reference case, in order to be used in the circular actuator model. This second boundary condition uses an empirical argument explained by Fig. 12 showing a schematic of Fig. 11. In Fig. 12, the discontinuous line represents the Discontinuous-Analytical case obtained with Eq. (22), and the continuous line represents the Continuous-FE case. For a given actuation stretch, the difference between the discontinuous and continuous stresses, ΔS_2, is assumed proportional to the difference between the discontinuous and pre-stretch stresses, ΔS_1. The quasi-linearity of the results of Fig. 11 suggests that the proportionality approximation is valid over significant actuation stretches. The proportionality relationship $\Delta S_2 \propto \Delta S_1$ is written with the terms of Fig. 12 as:

$$S_{\substack{1,\mathrm{act}\\ \mathrm{discontinuous}}} - S_{\substack{1,\mathrm{act}\\ \mathrm{discontinuous}}} = k\left(S_{1,\mathrm{pre}} - S_{\substack{1,\mathrm{act}\\ \mathrm{discontinuous}}}\right) \tag{23}$$

where k is the proportionality constant. Substituting $S_{\substack{1,\mathrm{act}\\ \mathrm{discontinuous}}}$ from Eq. (22) and rearranging gives the boundary condition used in the circular actuator model:

$$S_{\substack{1,\mathrm{act}\\ \mathrm{discontinuous}}} = S_1(R_a) - k(S_{1,\mathrm{pre}} - S_1(R_a)) \tag{24}$$

The proportionality constant was chosen to be $k = 1.6$ based on two criteria: (1) the predictions should follow the Continuous-FE levels of Fig. 11 and (2) the predictions should give realistic actuation area expansion levels compared to experimental values (see Fig. 19).

The boundary condition of Eq. (24) is expressed in the actuated configuration by the Piola transformation, see Eq. (12):

$$\sigma_{1,\mathrm{act}} = [S_1(R_a) - 1.6(S_{1,\mathrm{pre}} - S_1(R_a))]\lambda_{1,\mathrm{tot}} \tag{25}$$

The effect of working load is included in the boundary condition by adding a radial loading stress, σ_{load}, to Eq. (25):

$$\sigma_{1,\mathrm{act}} = [S_1(R_a) - 1.6(S_{1,\mathrm{pre}} - S_1(R_a))]\lambda_{1,\mathrm{tot}} + \sigma_{\mathrm{load}} \tag{26}$$

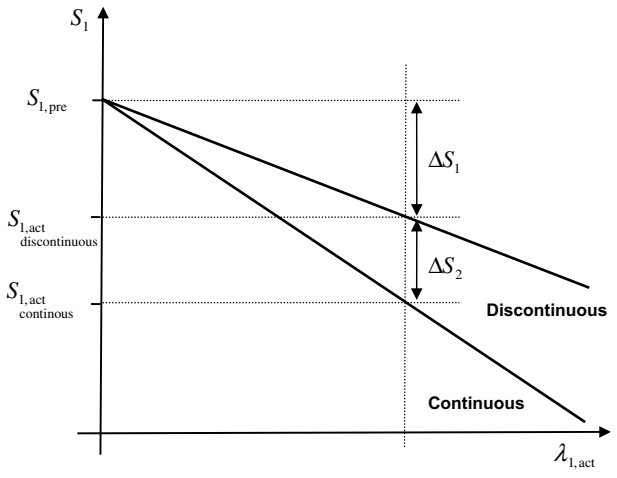

Fig. 12. Evolution of the planar stress in the active region during actuation.

This loading stress is compressive (negative) and thus block the film's expansion. Typical values of this loading stress at low and high stretch rates are estimated from diamond actuators (see Fig. 3) in Appendix C. Finally, the boundary condition of Eq. (26) is inserted back into Eq. (16) to complete the circular actuator model.

2.5. Failure criteria

Three failure modes are considered independently: material strength, dielectric strength, and pull-in, see Fig. 13. This paper uses simple descriptions of these failure modes to keep the analytical model tractable. Each of these failure modes should be investigated in greater detail by future studies. Failures that result from localized effects such as material defects, stress concentration, and field concentration are not considered here (for more information, see Vogan, 2004; Plante, 2006).

The failure modes study focuses on the active region of the film. The discussion is made in terms of area expansion ratio, which is equal to the inverse of the third principal stretch and to the square of a first principal stretch:

$$\frac{A_{\text{final}}}{A_{\text{initial}}} = \frac{1}{\lambda_3} = \lambda_1^2 \tag{27}$$

2.5.1. Material strength

In first approximation, material strength failure is assumed to be affected principally by film stretch. Effects of stress and stretch rate are not considered. The proposed failure mechanism is that film tearing occurs when folded polymer chains are straightened beyond their unfolded length. Hence, film deformation is limited to an experimentally determined maximum area expansion. Experiments suggest a value of 36 for VHB 4905/4910, leading to the following failure criterion:

$$\lambda_{1,\text{tot}}^2 > 36 \tag{28}$$

Kofod et al. (2001) and Larsen et al. (2002) have also proposed 36 as a safe practical area expansion limit for this material.

2.5.2. Dielectric strength

The breakdown voltage limit of a dielectric material is generally obtained experimentally. Polymer conductivity such as described by Whithead (1953) suggests that predicting dielectric failure requires representing complex molecular and atomic interactions and is not tractable. Dielectric failure is thus predicted from an empirical breakdown voltage vs. area expansion obtained for rigid, non-deforming electrodes (see Fig. 16). The maximum actuation area expansion as limited by dielectric strength is obtained when the model's electric field is higher than the mean experimental dielectric strength:

$$E > E_{\text{EXP}}(\lambda_{1,\text{tot}}^2) \tag{29}$$

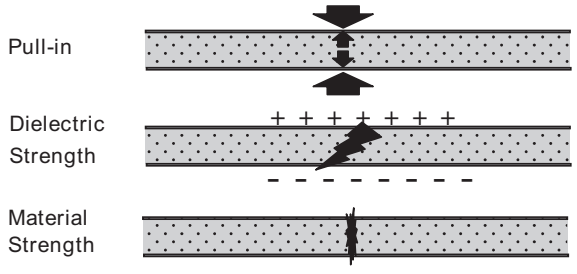

Fig. 13. Failure modes of DEA.

2.5.3. Pull-in instability

Pull-in instability appears when the equilibrium condition of Eq. (8) cannot be reached because the Maxwell pressure, P, becomes always greater than the film third principal stress $\sigma_{3,\mathrm{act}}$. The film typically collapses into complex 3D wrinkling patterns such as shown in Fig. 14. These wrinkles are seen before pull-in failure, although stable wrinkles can be observed under particular conditions (high pre-stretch, no working load). The excessive local deformations caused by pull-in eventually lead to either material or dielectric strength failures. It is the unstable approach to failure that makes pull-in a mode of its own. This study considers a simplified one-dimensional model that predicts the onset of pull-in instability. Further, it is assumed that if pull-in instability starts, voltage will not be removed and pull-in will eventually lead to failure.

For a given pre-stretch, the pull-in threshold is found by analyzing the equilibrium between the two stresses as shown in Fig. 15 for $\dot{\lambda}_{\mathrm{UNI}} = 3.3 \times 10^{-4}\ \mathrm{s}^{-1}$ and $\lambda^2_{1,\mathrm{pre}} = 3.86$. The third principal stress, $\sigma_{3,\mathrm{act}}$, obtained from Eq. (16) is plotted as a function of actuation stretch. Also shown are the equivalent Maxwell pressures, P, obtained from Eq. (1) at three different voltages as a function of actuation stretch. The location of the ultimate actuation stretch before pull-in is at the value of the tangent point of the *last* Maxwell pressure curve, P, to intersect the film's third principal stress curve, $\sigma_{3,\mathrm{act}}$. Voltages below the critical pull-in voltage are stable while those above are unstable. Fig. 15 shows that voltage V_1 has a stable solution, V_3 would result in pull-in, and voltage V_2 is the critical pull-in voltage for this material and pre-stretch.

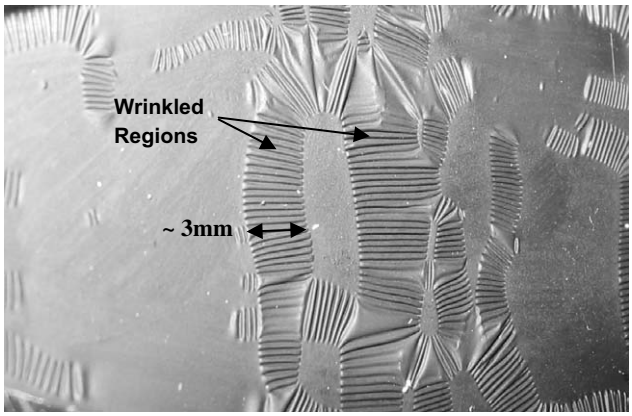

Fig. 14. Film geometry during pull-in instability.

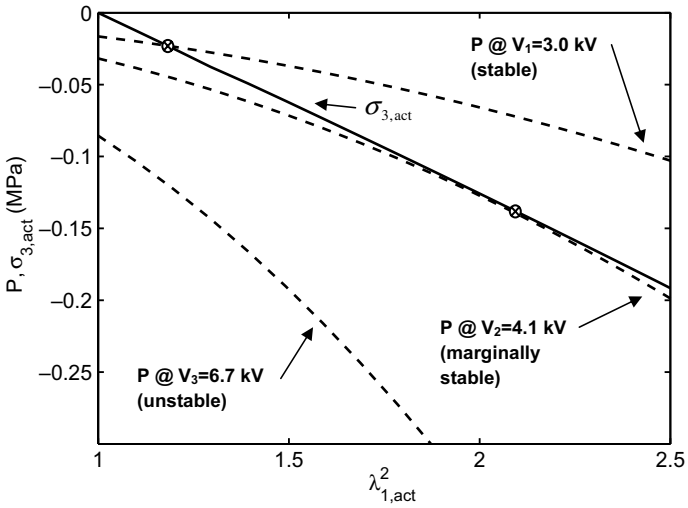

Fig. 15. Example of pull-in failure criterion.

As shown in Fig. 15, the location of the equilibrium point determining the occurrence of pull-in failures is very sensitive to the material's third principal stress response. At the same time, VHB 4905/4910 is a highly viscoelastic material whose stress levels are strongly affected by stretch rate, see Appendix A. Hence, it is reasonable that pull-in failure is strongly affected by stretch rate.

3. Experimental data

Laboratory experiments were performed to measure the maximum area expansion at failure of DEAs in order to validate the model and failure criteria developed in this paper. Experiments were done at both low ($\dot{\lambda}_{\mathrm{UNI}} = 3.3 \times 10^{-4}\ \mathrm{s}^{-1}$) and at high ($\dot{\lambda}_{\mathrm{UNI}} = 0.094\ \mathrm{s}^{-1}$) stretch rates, for circular actuators (no working load) and diamond actuators (with working load). Priority was set on high stretch rates where actuation periods are on the order of seconds rather than hours. Such time scales are representative of most practical robotic and mechatronic applications.

3.1. Circular actuators

Circular actuators were created in the center of large pre-stretched films. Electrodes were created as 10×10 mm squares instead of circles because they can reliably and rapidly be generated by intersecting two lines, one on each side of the film. The shape difference is not expected to be significant for the precision required by this study. The necessity for rapid actuator manufacturing is motivated by the fact that, at high stretch rates ($\dot{\lambda}_{\mathrm{UNI}} = 0.094\ \mathrm{s}^{-1}$), the film must be pre-stretched, electrodes created and voltage applied in a relatively short time ($\sim$5 min) in order to respect the constant stretch rate assumption.

In all tests, a sample of VHB 4905/4910 was pre-stretched in two perpendicular directions as described in Appendix B. Compliant electrodes were created with a conducting water based gel. Voltage was applied to the electrodes and increased with a Matsusada U3A-10P DC–DC voltage converter until failure was observed. The voltage application rate was selected to match the uniaxial test stretch rates.

At low stretch rates, electrode expansion is slow enough to enable continuous measurement of compliant electrode dimensions directly on the film. However, at high stretch rates, the electrode boundary is constantly moving and its dimensions at failure are difficult to measure. Optical methods are cumbersome and do not detect any film out-of-plane deformation (wrinkling) that might occur at high actuation stretches. Hence, an indirect method was developed here to infer area expansion at failure from breakdown voltage measurements.

In this method, the polymer film is stretched to given values and then sandwiched between a set of rigid electrodes. A voltage is then applied and gradually increased until arcing occurs across the material (dielectric breakdown). In this way the material's breakdown voltage as function of stretch state can be determined. The rigid electrodes maintain the constant stretch state of the material. In contrast, if voltage is applied with compliant electrodes, its stretch state will change. The stretch states at failure can be estimated from the calibration obtained with the rigid electrodes that gives the breakdown voltage vs. stretch states. The difference in stretch states between the rigid and compliant cases is the actuation stretch.

Fig. 16 shows the experimental voltage as a function of area pre-stretch for rigid and compliant electrodes at high stretch rate. The compliant electrodes curve was obtained from 28 points. The rigid electrode curve was determined from 45 points and is compared with data extrapolated from Kofod et al. (2001). The comparison shows good agreement except at $\lambda^2_{1,\mathrm{pre}} = 1.0$, which is off by a factor of two due to an error in the presentation of the paper (Verified by private communication with Kofod, 4/11/2003).

The experimental actuation area expansion to failure is plotted vs. pre-stretch area expansion at high stretch rates is shown in Fig. 17 with error boundaries of $\pm 30\%$ representing an estimate of experimental data scatter range. The mean curve of Fig. 17 appears smooth because it is obtained from the two data curve-fits of Fig. 16. The experimental curve of Fig. 17 appears lower than best values reported by Pelrine et al. (2000a,b). The experimental curve may represent a conservative average of DEA performance, assuming the reported values in the literature were obtained at similar stretch rates.

At low stretch rates, experimental data was obtained at three different pre-stretches. Each case was repeated four times and the average values are presented in Table 1. Table 1 and Fig. 17 show that experimental actuation area expansion is maximized for pre-stretches of about 10 for both low and high stretch rates.

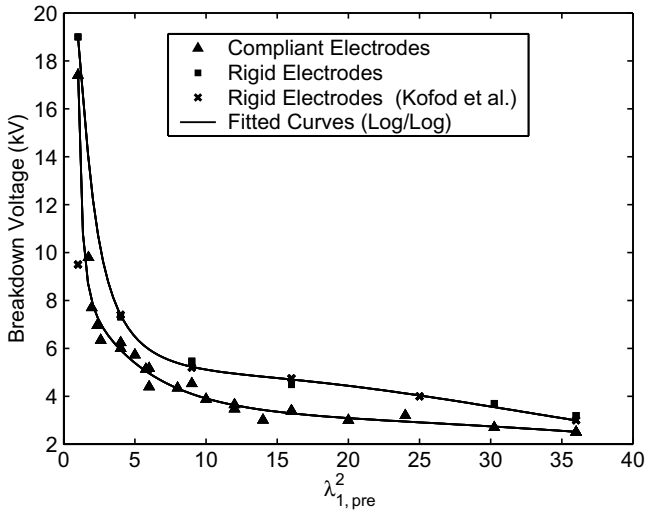

Fig. 16. Experimental breakdown voltages for rigid and compliant electrodes measured at high stretch rate ($\dot{\lambda}_{UNI} = 0.094\ s^{-1}$).

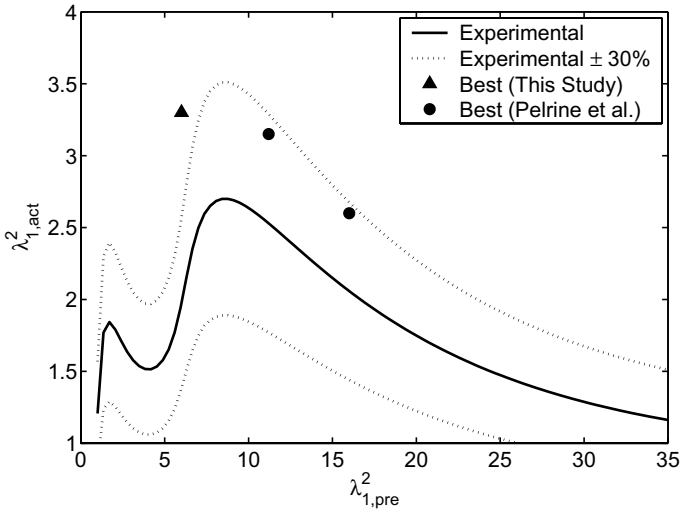

Fig. 17. Experimental ultimate actuation area expansion vs. pre-stretch area expansion at high stretch rate ($\dot{\lambda}_{UNI} = 0.094\ s^{-1}$).

Table 1
Experimental area expansion at failure for low stretch rate, $\dot{\lambda}_{UNI} = 3.3 \times 10^{-4}\ s^{-1}$

$\lambda^2_{1,pre}$	$\lambda^2_{1,act}$	$\min(\lambda^2_{1,act})$	$\max(\lambda^2_{1,act})$	Observed failure mode
5	1.77	1.60	1.92	Pull-in
10	4.29	3.50	4.60	Dielectric or material
16	2.86	2.25	3.36	Dielectric or material

3.2. Diamond actuators

Ten diamond actuators using 1.5 mm thick laminates of 4905 films were manufactured. Film pre-stretches of $[\lambda_{1,pre}, \lambda_{2,pre}] = [5,2.2]$ in the major/minor axis directions were used for a total pre-stretched area expansion ratio of 11. Experience in designing and manufacturing these actuators showed pre-stretches of 11 to give

maximum expansion before failure. Interestingly, this value is almost identical to the optimum value of 10 suggested in Fig. 17 and Table 1 for circular actuators.

The diamond actuators were pulled at constant velocity (see Plante (2006) for more details on the testing apparatus) with an applied voltage of 10 kV up to an area expansion of 2.28 (linear actuator strain of 150%). The samples were first pulled at high stretch rate and none of them failed. The same samples were then pulled for a second time at low stretch rate and it was observed that all 10 failed. Cumulative damage is considered negligible over only two cycles. At low stretch rates, the average area expansion at failure was 1.28 (linear actuator strain of 30%) with a lowest value of 1.05 (linear actuator strain of 6%). All failures showed the characteristic wrinkles of Fig. 14.

4. Model validation

The circular actuator model and its failure criteria were used to predict the ultimate actuation expansion vs. pre-stretch, with and without loading stresses, at low and high stretch rates ($\dot{\lambda}_{\mathrm{UNI}} = 3.3 \times 10^{-4}\ \mathrm{s}^{-1}$ and $0.094\ \mathrm{s}^{-1}$). In these predictions, voltage is increased until any of the three failure criteria are met (if met). The prediction results are now compared with experimental data. A short discussion about the impact of failure on DEA technology is provided.

4.1. Model vs. circular actuators (no working load)

At low stretch rates, the model predicts that failure can be caused by any of the three modes, depending on pre-stretch, see Fig. 18. Dielectric strength failure is only apparent at very low pre-stretches that are not used in practice. Pull-in failure dominates the low pre-stretch range up to pre-stretches of about 10. For pre-stretches above 10, the pull-in instability criterion is not met anymore and failure is dominated by material strength. When pull-in failures are possible, the maximum area expansion is limited to a relatively constant value of about 1.9. This value is not very far from the linear (Hookean) model predictions discussed in the introduction, giving a limit of 1.6, see Pelrine et al. (1998), Kornbluh et al. (1999), and Sommer-Larsen et al. (2001). This is likely because at low rates, the equilibrium stress/stretch curve is almost linear, see Fig. 22 of Appendix A. The model agrees well with experimental data. On the figure, the vertical lines across experimental points represent data scatter. As pre-stretch increases beyond a certain threshold of about $\lambda^2_{1,\mathrm{pre}} = 9$, the pull-in failure mode disappears, allowing very large actuation area expansions, up to 4.29 at $\lambda^2_{1,\mathrm{pre}} = 10$.

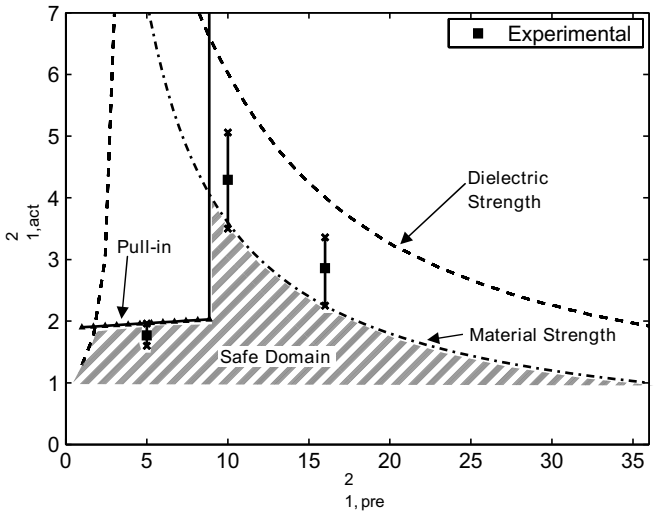

Fig. 18. Failure analytical predictions for low stretch rate ($\dot{\lambda}_{\mathrm{UNI}} = 3.3 \times 10^{-4}\ \mathrm{s}^{-1}$) compared with experimental values.

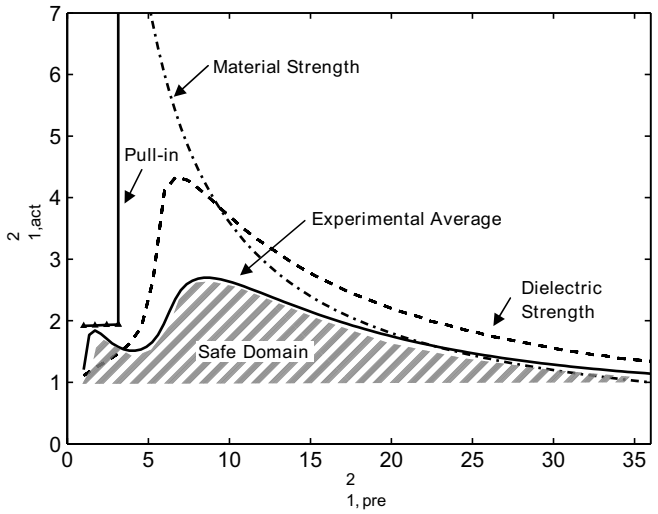

Fig. 19. Failure analytical predictions for high stretch rate ($\dot{\lambda}_{\mathrm{UNI}} = 0.094\ \mathrm{s}^{-1}$) compared with experimental values.

At high stretch rates, the model predicts that failure can be caused only by two modes, see Fig. 19. Dielectric strength is the limiting factor for pre-stretches below 10. For pre-stretches above 10, material strength is the limiting factor. The experimental curve is bounded by the failure criteria. Low pre-stretches failures are bounded by dielectric strength effects and large pre-stretch by material strength. The model and experimental curves both show an optimum pre-stretch at about 10. In the pre-stretch range of 5–15, the model over-predicts the maximum actuation area expansion (4.25 vs. 2.7). This discrepancy is principally attributed to the simplicity of the passive region model that uses an empirical boundary condition not included in the elastic deformation theory.

4.2. Model vs. diamond actuators (with working load)

The failure predictions are compared with experimental data of the 10 diamond actuators in Figs. 20 and 21, respectively, for low and high stretch rates. The predictions show the same general trends as in Figs. 18 and

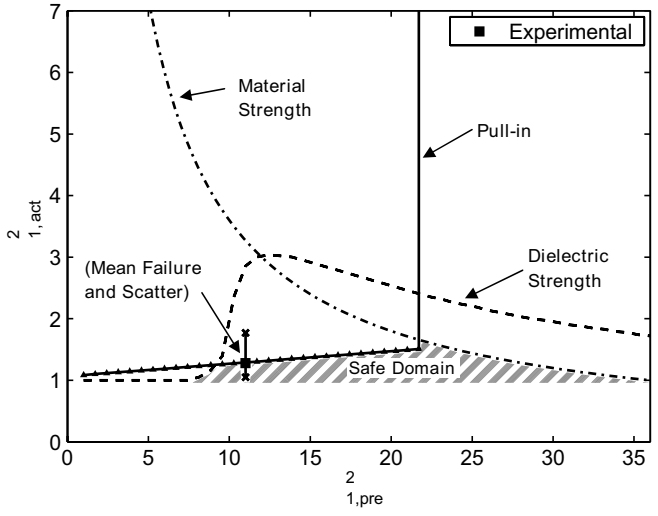

Fig. 20. Failure analytical predictions for low stretch rate ($\dot{\lambda}_{\mathrm{UNI}} = 3.3 \times 10^{-4}\ \mathrm{s}^{-1}$) with loading stress compared with experimental values of 10 diamond actuators.

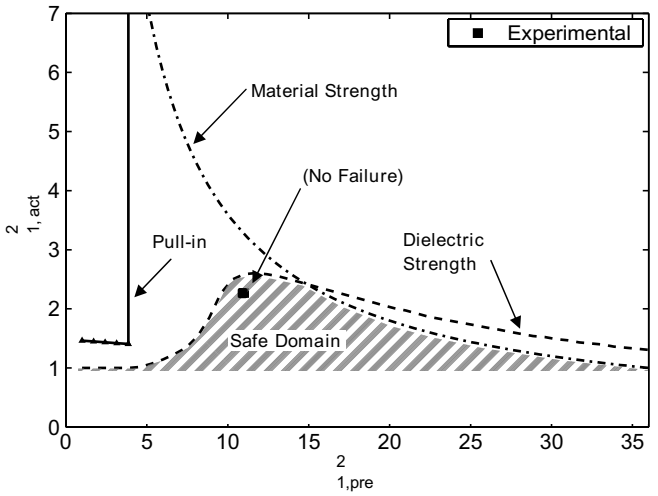

Fig. 21. Failure analytical predictions for high stretch rate ($\dot{\lambda}_{\mathrm{UNI}} = 0.094\ \mathrm{s}^{-1}$) with loading stress compared with experimental values of 10 diamond actuators.

19. The model predictions corroborate well the data showing severe pull-in limitations at low stretch rates. Based on these results, it appears that DEAs operating under working loads are severely limited by pull-in failure compared to unloaded actuators.

4.3. Discussion

In general, model predictions agree well with experimental data, with and without working loads, at both low and high stretch rates. The model explains the behavior of the three postulated failure modes and explains observed experimental trends. The model is valid for unidirectional stretches of up to 6.

The principal limitation of the proposed model is its incapacity to represent the geometry of the interface between the active and passive regions. An in-depth multi-physics FE model coupling electrostatics and solid mechanics would be required to accurately represent the true interface shape. Also, the model flexibility is limited as it is only defined for two constant stretch rates.

The key result shown by the model is the positive impact of viscoelasticity on reliability. Viscoelasticity significantly affects the amount of viscous impedance at high stretch rates, see Appendix A. These viscous forces "stiffen" the film and protect it from pull-in failures. In contrast, low stretch rates generate less viscous impedance and pull-in failure dominates.

This viscous impedance has a significant impact on performance when working loads are considered. For example, the maximum linear actuator strains of diamond actuators is five times higher at high stretch rates compared to low stretch rates: 150% vs. 30% (see Figs. 20 and 21). The difference is not as great for circular actuators operating without working loads (see Figs. 18 and 19). Hence, working loads cannot be neglected in DEA analysis and design.

The model shows that pull-in failure is a limitation of DEAs based on VHB 4905/4910. Controlling the position of such actuators under working loads for long time scales is not likely to be possible at large extensions. One possible application of DEA that does not require continuous state holding is binary robotics using bi-stable actuators such as proposed by Vogan (2004) and Plante et al. (2005). In this application, DEAs are powered only for short duration and operate only under high stretch-rate conditions, thus maximizing their achievable actuation stretches and reliability. Bi-stable elements perform the long-duration position holding.

5. Conclusions

A model of dielectric elastomer actuation was developed using a continuum mechanics framework for hyper-elastic materials. Rate-dependent effects were captured by specifying different material properties for

different stretch rates. Three large-scale failure criteria were established: material strength, dielectric strength and pull-in. These criteria were used in conjunction with the actuation model to predict ultimate area expansion of circular actuators at two different stretch rates, with and without working loads. The predictions were corroborated experimentally on circular and diamond actuators showing that working loads have a significant impact on actuator failure and cannot be neglected.

An important conclusion of this study is that DEAs using VHB 4905/4910 (or similar viscoelastic materials) have failure modes and performance boundaries that depend strongly on stretch rate. Viscoelasticity plays an important role in preventing pull-in failures by "stiffening" the film. This study leads to the following guidelines and performance boundaries defined for DEAs made with VHB 4905/4910:

1. Dielectric strength failure is the dominant mode of failure under high stretch rates. In contrast, pull-in instability is the performance limiter at low stretch rates.
2. When operating at low stretch rates under load, actuation area expansion is limited to about 1.28 regardless of the pre-stretch (see Fig. 20), giving linear actuator strains of about 30% for diamond actuators.
3. When operating at high stretch rates under load with pre-stretched area expansions of 10–15, actuation area expansions of up to 2.5 are possible (see Fig. 21), giving linear actuator strains of about 150% for diamond actuators.
4. Practical actuators can only operate reliably under high loads in fast, intermittent or high-frequency applications.

Extrapolation of these results to other actuator designs should be done with care. Finally, the failure modes study presented in this paper revealed the properties of ideal DEA films, which still need to be developed:

1. Properly tuned stress/stretch behavior, just enough to prevent pull-in failures.
2. Little or no viscoelastic effects (unless viscous impedance prevents pull-in failure, like VHB 4905/4910).
3. Highest possible dielectric strength to prevent dielectric strength failures.
4. Highest possible extensions to prevent material strength failures.
5. Highest dielectric constant to maximize Maxwell pressure.
6. Lowest level of defects and contaminants to ensure consistency.

Acknowledgments

This work was done with sponsorship of the Cambridge-MIT Institute (CMI), the Center for Integration of Medicine and Innovative Technology (CIMIT), and the NASA Institute for Advanced Concepts (NIAC). The authors extend their thanks to Professors M. Boyce and R. Abeyaratne for their valuable discussions, and to Sam Korb for his contribution to experimental work. Thanks also to Dr. M. Lichter for his valuable inputs.

Appendix A. Material properties

A.1. Uniaxial stress formulation

Consider a rectangular sample in uniaxial deformation along its first principal direction. The principal stretches for an incompressible material like VHB 4905/4910 are given by:

$$\lambda_1 = \frac{l}{l_0}$$
$$\lambda_2 = \lambda_3 = \lambda_1^{-0.5} \tag{30}$$

where l_0 and l are the sample lengths in the reference and deformed configurations.

The corresponding stresses in the reference configuration given by a second order Ogden model are:

$$S_1 = \mu_1 \lambda_1^{(\alpha_1 - 1)} + \mu_2 \lambda_1^{(\alpha_2 - 1)} - \mu_1 \lambda_1^{-(1+0.5\alpha_1)} - \mu_2 \lambda_1^{-(1+0.5\alpha_2)}$$
$$S_2 = S_3 = 0 \tag{31}$$

The first principal stress, S_1, vs. stretch function of Eq. (31) was fitted on experimental data to by adjusting the Ogden parameters α_1, α_2, μ_1, μ_2 using the NonlinearRegress function in the Mathematica® Software.

A.2. Experimental data

The specimen's nominal clamped dimensions were arbitrarily set to 15×15 mm and their final dimensions were measured with a Mitutoyo caliper. Stresses and stretches were measured on a custom tensile test machine using an Omega LCEB-5 5 lbf load cell.

Uniaxial tests with different stretch rates were performed to investigate viscoelastic effects. Fig. 22 shows filtered experimental data of the stresses vs. stretches for four different stretch rates, $\dot{\lambda}_{\mathrm{UNI}}$, ranging from $3.1 \times 10^{-5}\,\mathrm{s}^{-1}$ to $1.8\,\mathrm{s}^{-1}$. The stretch rate $\dot{\lambda}_{\mathrm{UNI}} = 3.3 \times 10^{-4}\ \mathrm{s}^{-1}$, (c), is interesting because it represents the equilibrium case where viscoelastic effects are negligibly small and the material response is mostly elastic (independent of stretch rate). As shown by Fig. 22, curves (c) and (d) are almost identical despite curve (d) having a stretch rate 10 times lower. The dashed curves superimposed on (a), (b) and (c) are curve-fitted Ogden models. Table 2 summarizes the Ogden model parameters that are valid for unidirectional stretches of up to 7.

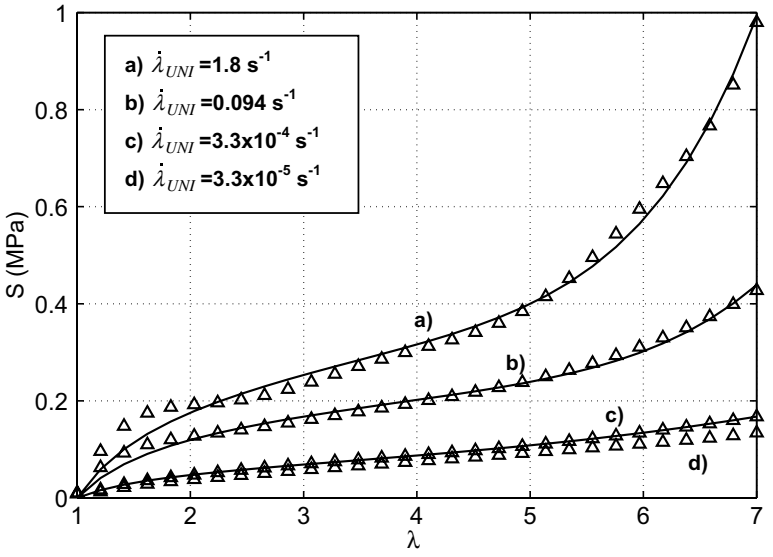

Fig. 22. Experimental stress/stretch curves for uniaxial extension of VHB 4905/4910 at different stretch rates. The solid curves on (a), (b) and (c) are curve-fitted Ogden models.

Table 2
Ogden model parameters from uniaxial tests

Ogden parameters	Low stretch rate, $\dot{\lambda}_{\mathrm{UNI}} = 3.3 \times 10^{-4}\ \mathrm{s}^{-1}$	High stretch rate, $\dot{\lambda}_{\mathrm{UNI}} = 0.094\,\mathrm{s}^{-1}$
α_1	1.445	1.450
α_2	4.248	8.360
μ_1	43,560	112,200
μ_2	117.4	0.1045

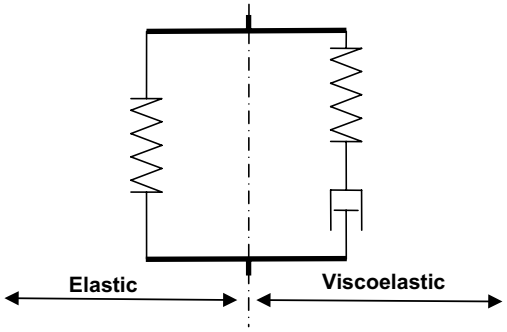

Fig. 23. Springs and dash-pot model for viscoelastic elastomers.

Viscoelastic materials are often represented with a rheologic model such as illustrated in Fig. 23. Under high stretch rates, significant viscous stresses are generated on the viscoelastic side of the rheologic model. These viscoelastic stresses add to the baseline elastic stresses and explain the viscous impedance observed in Fig. 22. For example, compare the stresses of curve (b) to curve (c) at a stretch of about 6. The stress of curve (c), the equilibrium case, is only 50% of the stress of curve (b). Thus, under high stretch rates, viscous stresses can account for more than half the total stress.

Appendix B. Stretching technique

B.1. Procedure

Pre-stretching is done with a two axis (Cartesian) stretching device. Pre-stretching must be executed in two steps due to the very high stretch values. The film sample is first clamped across one axis and the initial dimensions, L and W, are measured such as in Fig. 24a. Next, the length is increased to the desired stretch in the first direction:

$$l = L\lambda_{1,\mathrm{pre}} \tag{32}$$

After obtaining the configuration shown in Fig. 24b, the free edges are clamped with the second set of clamps, see Fig. 24c. The free width of the sample, w_a, and the clamped width, w_b, are measured. To account for the amount of clamped material, the initial length in the secondary axis is linearly scaled:

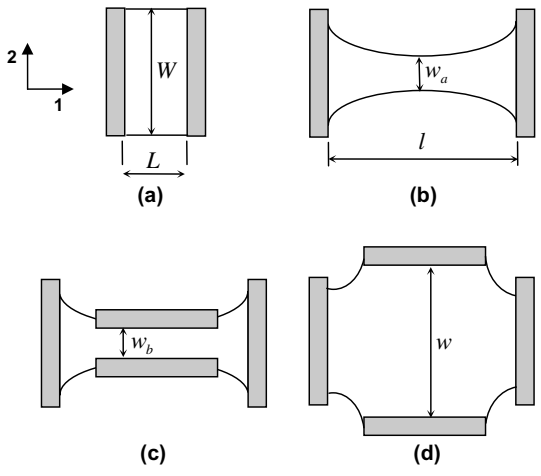

Fig. 24. Stretching sequence.

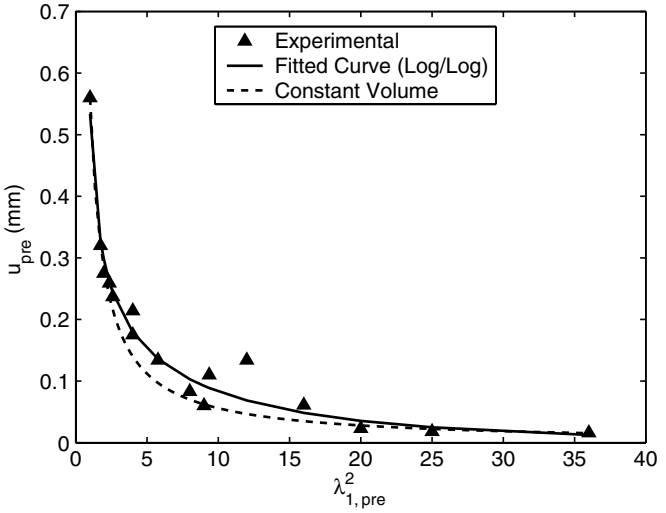

Fig. 25. Experimental vs. constant volume film thickness.

$$W' = \frac{w_b}{w_a} W \tag{33}$$

By expanding the clamped edges, the film is then brought to its final stretched configuration as shown in Fig. 24d where the final width is obtained from the second direction stretch:

$$w = \lambda_{2,pre} W' \tag{34}$$

B.2. Validation

Stretching elastomer films to large values causes film slippage problems. Therefore, to verify that the final stretches are valid, the resulting thickness was measured and compared with the thickness calculated by the constant volume assumption. Multiple elastomer samples were stretched and their final thickness was measured with a Mitutoyo torque limited micrometer (model # 293-761-30). The measurements are plotted against predictions from the constant volume assumption in Fig. 25. The scattering of midrange data is attributed to slight film slippage from under the clamps, which results in higher measured thickness. The data scattering disappears for high pre-stretch because film slippage becomes small in comparison with the total film area. In general, experimental data match well the constant volume curve. Therefore, the stretching technique is considered adequate for the scope of this work.

Appendix C. Diamond actuator loading stress

A typical loading stress function is estimated from force measurements performed on diamond actuators such as schematized in Fig. 26 where l is the diamond side length, u is the film thickness and θ is the diamond half angle. The actuators consisted of a single 1.5 mm thick film pre-stretched to $[\lambda_{1,pre}, \lambda_{2,pre}] = [5, 2.2]$ and mounted to a $l = 55$ mm diamond actuator frame operating between $\{u = 0.14\text{ mm},\ \theta = 9°\}$ and $\{u = 0.06\text{ mm}, \theta = 24°\}$. Actuation area expansion is 2.28. Experimental measurements (Plante, 2006) showed that, at 10 kV, the loading force ($F_{load} = F_{Voltage\,OFF} - F_{Voltage\,ON}$) of these diamond actuators is approximately constant for a given stretch rate:

- $F_{load} \sim 1.75$ N at low stretch rates, $\dot{\lambda}_{UNI} = 3.3 \times 10^{-4}\ s^{-1}$.
- $F_{load} \sim 0.875$ N at high stretch rates, $\dot{\lambda}_{UNI} = 0.094\ s^{-1}$.

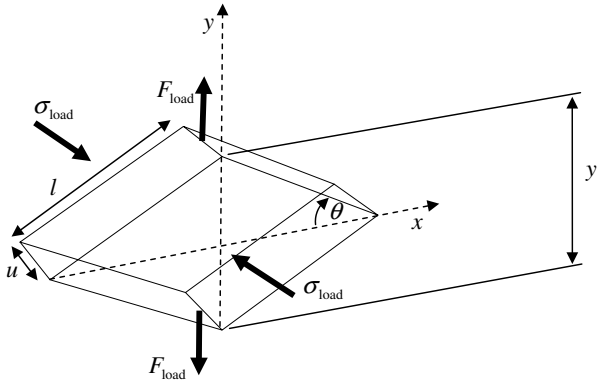

Fig. 26. Diamond actuator loading stress.

The authors showed (Plante, 2006) that the compressive loading stress, σ_{load}, of diamond actuators is related to the actuator loading force, F_{load}, by

$$\sigma_{load} = -\frac{F_{load}}{lu\cos\theta(\tan^2\theta - 1)} \tag{35}$$

According to Eq. (35), the loading stress varies from $\sigma_{load} = -0.14F_{load}$ in the closed configuration to $\sigma_{load} = -0.42F_{load}$ in the opened configuration. The loading stress variation with area expansion is transposed linearly to circular actuators by:

$$\sigma_{load} = [0.56(1 - \lambda_{1,act}) - 0.14]F_{load} \tag{36}$$

where $\lambda_{1,act}$ is the radial actuation stretch. For example, a diamond actuator operating at an actuation area expansion of 2.28 corresponds to a circular actuator operating at $\lambda_{1,act} = \sqrt{2.28} = 1.5$ which, when inserted into Eq. (36), yields the same loading stress of $\sigma_{load} = -0.42F_{load}$.

References

3M, 2001. VHB Double Coated Acrylic Foam Tapes and Adhesives Transfer Tapes. 3M™ VHB.pdf, Technical Data, 13p.

Anand, L., 1996. A constitutive model for compressible elastomeric solids. Computational Mechanics 18, 339–355.

Anand, L., Gurtin, M.E., 2003. A theory of amorphous solids undergoing large deformations, with application to polymeric glasses. International Journal of Solids and Structures 40, 1465–1487.

Bergström, J., Boyce, M., 1998. Constitutive modeling of the large strain time-dependant behavior of elastomers. Journal of Mechanics and Physics of Solids 46 (5), 931–954.

Bergström, J., Boyce, M., 2000. Large strain time-dependant behavior of filled elastomers. Mechanics of Materials 32, 627–644.

Cameron, C., Underhill, R., Rawji, M., Szabo, J., 2004. Conductive filler – elastomer composites for Maxwell stress actuator applicationsProceedings of Smart Structures and Materials 2004: Electroactive Polymer Actuators and Devices (EAPAD), vol. 5385. SPIE, San Diego, CA, pp. 51–59.

Drozdov, A.D., Dorfmann, A., 2002. The nonlinear viscoelastic response of carbon black-filled natural rubbers. International Journal of Solids and Structures 39, 5699–5717.

Goulbourne, N., Frecker, M., Mockensturm, E., Snyder, A., 2003. Modeling of a dielectric elastomer diaphragm for a prosthetic blood pumpProceedings of Smart Structures and Materials 2003: Electroactive Polymer Actuators and Devices (EAPAD), vol. 5051. SPIE, San Diego, CA, pp. 319–331.

Goulbourne, N., Frecker, M., Mockensturm, E., 2004. Electro-elastic modeling of a dielectric elastomer diaphragm for a prosthetic blood pumpProceedings of Smart Structures and Materials 2004: Electroactive Polymer Actuators and Devices (EAPAD), vol. 5385. SPIE, San Diego, CA, pp. 122–133.

Holzapfel, G.A., 2000. Nonlinear Solid Mechanics. Wiley, Chichester, UK.

Kofod, G., 2001. Dielectric Elastomer Actuators. Ph.D. Thesis, Department of Chemistry, The Technical University of Denmark, Denmark.

Kofod, G., Kornbluh, R., Pelrine, R., Sommer-Larsen, P., 2001. Actuation response of polyacrylate dielectric elastomersProceedings of Smart Structures and Materials 2001: Electroactive Polymer Actuators and Devices (EAPAD), vol. 4329. SPIE, San Diego, CA, pp. 141–147.

Kofod, G., Sommer-Larsen, P., 2005. Silicone dielectric elastomer actuators : finite-elasticity model of actuation. Sensors and Actuators 122, 273–283.

Kornbluh, R., Pelrine, R., Joseph, J., 1995. Elastomeric dielectric artificial muscle actuators for small robots. In: Proceedings of the Materials Research Society Symposium, vol. 600, pp. 119–130.

Kornbluh, R., Pelrine, R., Joseph, J., Heydt, R., Pei, Q., Chiba, S., 1999. High-field electrostriction of elastomeric polymer dielectrics for actuationProceedings of Smart Structures and Materials: Electroactive Polymer Actuators and Devices, vol. 3669. SPIE, New Port Beach, CA, pp. 149–161.

Kornbluh, R., Pelrine, R., Pei, Q., Oh, S., Joseph, J., 2000. Ultrahigh strain response of field-actuated elastomeric polymersProceedings of Smart Structures and Materials: Electroactive Polymer Actuators and Devices, vol. 3987. SPIE, San Diego, CA, pp. 51–64.

Kornbluh, R., Pelrine, R., Pei, Q., Heydt, R., Stanford, S., Oh, S., Eckerle, J., 2002. Electroelastomers: Applications of dielectric elastomer transducers for actuation, generation and smart structuresProceedings of Smart Structures and Materials 2002: Electroactive Polymer Actuators and Devices (EAPAD), vol. 4698. SPIE, San Diego, CA, pp. 254–270.

Larsen, P., Kofod, G., Benslimane, M., Gravesen, P., Shridhar, M.H., 2002. Performance of dielectric elastomer actuators and materialsProceedings of Smart Structures and Materials 2002: Electroactive Polymer Actuators and Devices (EAPAD), vol. 4695. SPIE, San Diego, CA, pp. 158–166.

McMeeking, R., Landis, C., 2005. Electrostatic forces and stored energy for deformable dielectric materials. Journal of Applied Mechanics 72 (4), 581–590.

Ogden, R.W., 1972. Large deformation isotropic elasticity – on the correlation of theory and experiment for incompressible rubberlike solids. In: Proceedings of the Royal Society of London, vol. A326, pp. 565–584.

Ogden, R.W., 1982. Elastic deformations of rubberlike solids. In: Hopkins, H.G., Sewell, M.J. (Eds.), Mechanics of Solids. Pergamon Press, Oxford, pp. 499–537 (the Rodney Hill 60th Anniversary Volume).

Ogden, R.W., 1984. Non-Linear Elastic Deformations. Dover Publications, New York.

Pei, Q., Rosenthal, M., Pelrine, R., Stanford, S., Kornbluh, R., 2003. Multifunctional electroelastomer roll actuators and their application for biomimetic walking robotsProceedings of Smart Structures and Materials 2003: Electroactive Polymer Actuators and Devices (EAPAD), vol. 5051. SPIE, San Diego, CA, pp. 281–290.

Pei, Q., Pelrine, R., Rosenthal, M., Stanford, S., Prahlad, H., Kornbluh, R., 2004. Recent progress on electroelastomer artificial muscles and their application for biomimetic robotsProceedings of Smart Structures and Materials 2004: Electroactive Polymer Actuators and Devices (EAPAD), vol. 5385. SPIE, San Diego, CA, pp. 41–50.

Pelrine, R., Kornbluh, R., Joseph, J., 1998. Electrostriction of polymer dielectrics with compliant electrodes as a means of actuations. Sensor and Actuators A: Physical 64 (1), 77–85.

Pelrine, R., Kornbluh, R., Joseph, J., Heydt, R., Pei, Q., Chiba, S., 2000a. High-field deformation of elastomeric dielectrics for actuators. Materials Science & Engineering C: Biomimetic and Supramolecular Systems 11 (2), 89–100.

Pelrine, R., Kornbluh, R., Pei, Q., Joseph, J., 2000b. High speed electrically actuated elastomers with stretch greater than 100%. Science 287, 836–839.

Pelrine, R., Sommer-Larsen, P., Kornbluh, R., Heydt, R., Kofod, G., Pei, Q., Gravesen, P., 2001. Applications of dielectric elastomer actuatorsProceedings of Smart Structures and Materials 2001: Electroactive Polymer Actuators and Devices (EAPAD), vol. 4329. SPIE, San Diego, CA, pp. 335–349.

Plante, J.S., Santer, M., Pellegrino, S., Dubowsky S., 2005. Compliant bistable dielectric elastomer actuators for binary mechatronic systems. In: Proceedings of IDECT/CIE 2005: ASME Mechanism and Robotics Conference, Long Beach, CA, USA.

Plante, J.S., 2006. Dielectric Elastomer Actuators for Binary Robotics and Mechatronics. Ph.D. Thesis, Department of Mechanical Engineering, Massachusetts Institute of Technology, Cambridge, MA.

Sommer-Larsen, P., Hooker, J., Kofod, G., West, K., Benslimane, M., Gravesen, P., 2001. Response of dielectric elastomer actuatorsProceedings of Smart Structures and Materials 2001: Electroactive Polymer Actuators and Devices (EAPAD), vol. 4329. SPIE, San Diego, CA, pp. 157–163.

Sommer-Larsen, P., Ladeggard Larsen, A., 2004. Materials for dielectric elastomer actuatorsProceedings of Smart Structures and Materials 2004: Electroactive Polymer Actuators and Devices (EAPAD), vol. 5385. SPIE, San Diego, CA, pp. 68–77.

Vogan, J., 2004. Development of Dielectric Elastomer Actuators for MRI Devices. M.S. Thesis, Department of Mechanical Engineering, Massachusetts Institute of Technology, Cambridge, MA.

Vogan, J., Wingert, A., Hafez, M., Plante, J.S., Dubowsky, S., Kacher, D., Jolesz, F., 2004. Manipulation in MRI devices using electrostrictive polymer actuators: with an application to reconfigurable imaging coils. In: Proceedings – 2004 IEEE International Conference on Robotics and Automation, New Orleans, LA, vol. 2004, No. 3, pp. 2498–2504.

Whithead, S., 1953. Dielectric Breakdown of Solids. Oxford University Press, London, 271p..

Wingert, A., 2002. Development of a Polymer-Actuated Binary Manipulator. M.S. Thesis, Department of Mechanical Engineering, Massachusetts Institute of Technology, Cambridge, MA.

Wingert, A., Lichter, M.D., Dubowsky, S., 2002a. On the kinematics of parallel mechanisms with bi-stable polymer actuators. In: Proceedings of the 8th International Symposium on Advances in Robot Kinematics, Barcelona, Spain.

Wingert, A., Lichter, M., Dubowsky, S., Hafez, M., 2002b. Hyper-redundant robot manipulators actuated by optimized binary dielectric polymersProceedings of Smart Structures and Materials 2002: Electroactive Polymer Actuators and Devices (EAPAD), vol. 4695. SPIE, San Diego, CA, pp. 415–423.

Wissler, M., Mazza, E., 2005. Modeling of a pre-strained circular actuator made of dielectric elastomers. Sensors and Actuators 120, 184–192.

Yang, W.H., Feng, W.W., 1970. On axisymmetrical deformations of nonlinear membranes. Journal of Applied Mechanics 37 (4), 1002–1011.

Yang, E., Frecker, M., Morckensturm, E., 2005. Viscoelastic model of dielectric elastomer membranesProceedings of Smart Structures and Materials 2005: Electroactive Polymer Actuators and Devices (EAPAD), vol. 5759. SPIE, San Diego, CA, pp. 82–93.